On the Importance of Joint Mitigation Strategies for Front, Bulk, and
Rear Recombination in Ultrathin Cu(In,Ga)Se-2 Solar Cells
Peer-reviewed author version

On the importance of joint mitigation strategies for front, bulk and rear recombination in ultrathin Cu(In,Ga)Se2 solar cells.

Tomás S. Lopes[*,1,2,3,4]*, Jessica de Wild*[2,3,4]*, Célia Rocha*[1]*, André Violas*[1]*, José M.V. Cunha*[1,5,6]*,
Jennifer P. Teixeira[1]*, Marco A. Curado*[1,7]*, António J.N. Oliveira*[1]*, Jérôme Borme*[1]*, Gizem
Birant[2,3,4]*, Guy Brammertz*[2,3,4]*, Paulo Fernandes*[1,8]*, Bart Vermang*[2,3,4]*, Pedro M.P Salomé*[1,6]

[1]INL – International Iberian Nanotechnology Laboratory, Avenida Mestre José Veiga, 4715-330
Braga, Portugal

[2]Imec division IMOMEC (partner in Solliance), Wetenschapspark 1, 3590 Diepenbeek, Belgium

[3]Institute for Material Research (IMO), Hasselt University (partner in Solliance),
Agoralaangebouw H, Diepenbeek, 3590, Belgium

[4]EnergyVille, Thorpark, Poort Genk 8310 & 8320, 3600, Belgium

[5]i3N, Departamento de Física da Universidade de Aveiro, Campus Universitário de Santiago,
3810-193 Aveiro, Portugal

[6]Departamento de Física, Universidade de Aveiro, Campus Universitário de Santiago, 3810-193
Aveiro, Portugal

[7]University of Coimbra, CFisUC, Department of Physics, R. Larga, P-3004-516 Coimbra, Portugal

[8]CIETI, Departamento de Física, Instituto Superior de Engenharia do Porto, Instituto Politécnico do Porto, Porto 4200-072, Portugal

Abstract

Several optoelectronic issues, such as recombination and poor optical absorption limit the power conversion efficiency of ultrathin $Cu(In,Ga)Se_2$ (CIGS) solar cells. To mitigate recombination losses, we implement two combined strategies: a Potassium Fluoride (KF) Post-Deposition Treatment (PDT) and a rear interface passivation strategy based on a point contact structure consisting of Aluminium Oxide (Al_2O_3). Moreover, we study the influence of both of these processes on electrical parameters and recombination mechanisms. The simultaneous implementation of both treatments is reported for the first time on ultrathin CIGS devices. Electrical measurements and 1-D simulations demonstrate that, in specific conditions, rear interface passivation strategy leads to lower electrical performance when compared with devices with only a KF-PDT. By combining KF-PDT and rear interface passivation, an enhancement in open-circuit voltage of 178 mV is reached over devices that have a rear passivation only and of 85 mV over devices with a PDT process only. Time-Resolved Photoluminescence measurements showed the beneficial effects of combining KF-PDT and the rear interface passivation at decreasing recombination losses in the studied devices. The device with both treatments shows a charge carrier lifetime that is higher than the ones from the devices with individual treatments. Our results suggest that when bulk and front interface recombination values are very high, they dominate and individual passivation strategies do not work. Hence, this work shows that for ultrathin devices, passivation mitigation strategies need to be implemented in tandem.

Keywords : ultrathin CIGS, KF-PDT passivation, Al_2O_3 , recombination mechanisms

Introduction

In order for thin-film Cu(In,Ga)Se$_2$ (CIGS) solar cells to settle with the highest power conversion efficiency values among the thin-film technology, strategies to mitigate recombination at the semiconductor interfaces and in the absorber bulk had to be developed. In the technology infancy, efficiency enhancements came by improving the architecture developed by Boeing and by optimizing the fabrication process. [1–3] As the technology became more mature, with well-established fabrication process conditions, recombination losses were the major obstacle for further improvements in light to power conversion efficiency. Studies showed the presence of significant recombination losses in high-efficiency CIGS solar cells (~19 %) occurring in the absorber bulk and at the front surface. [4–6] Heavy alkali implementation via PDT helped the CIGS technology to achieve several world records, most recently it reached 23.35 % in power conversion efficiency.[7–11] In a PDT process, an alkali metal is deposited after the absorber deposition. Potassium (K) is one of the first successful PDTs in CIGS solar cells.[7] The excellent results of KF-PDT paved the way for other successful alkalis PDT, such as Cs and Rb[9–13], with a significant amount of studies being conducted to understand the effects of PDT on the properties of CIGS solar cells.[14–19] CIGS solar cells with PDT show standardly enhanced electrical performance.[7,15,20] Several reports show the influence of KF-PDT at improving the front surface as well as the CIGS bulk properties.[7,14–16,21,22] Looking to the CIGS/CdS interface, KF-PDT leads to a reduction of the amount of Cu and Ga[7,14,15,17] – that promotes Cd filling of copper vacancies (V_{cu}) during chemical bath deposition (CBD) resulting in a higher density of shallow Cd_{cu} donors.[7,23] This process allows for thinning the CdS layer without compromising

electrical performance and reducing the parasitic light absorption.[7,8,24] Such effects are linked with reduced front surface recombination leading to increased open-circuit voltage (V_{OC}) and fill factor (FF) values.[7,15] Effects of KF-PDT in the CIGS bulk properties were also reported with some effects being: KF accumulation at the grain boundaries[15,17,25], reducing tail states, leading to a reduction of band-bending in the grain boundaries, and thus promoting grain boundary passivation.[14]

One of the research lines in the CIGS community is to develop high efficiency ultrathin CIGS solar cells, without compromising performance, in order to save material costs and increase machine throughput.[26] However, in ultrathin CIGS solar cells, rear interface recombination is a major efficiency loss mechanism.[27–29] A strategy to mitigate rear interface recombination was developed in which a dielectric is deposited in-between the CIGS and the Molybdenum (Mo) rear electrode.[30] The dielectric reduces rear interface recombination by: i)neutralizing active recombination centres[31,32]; ii) and by a built-in electric field – created by fixed charges present in the dielectric and at the surface that shields minority carriers, therefore reducing recombination.[33] Among all the dielectrics used and studied so far, alumina oxide (Al_2O_3) has shown good results at reducing rear interface recombination.[34,35] The dielectric layer needs to be patterned to establish electrical contact between the CIGS and rear electrode creating a point contact structure. Patterning approaches by lithography[36–38] show controlled and reproducible results. Despite its success, there are reports, in which the use of a passivation layer decreases the device electrical performance with the conditions for such decrease being highly debatable among the community.[39–41] Due to the significant electronic losses at the rear interface, little attention was given to the implementation of PDT in ultrathin CIGS. However, recent reports show the beneficial effects of KF-PDT in ultrathin CIGS solar cells,

with devices attaining enhanced electrical performance.[20,42] The recent results with KF-PDT in ultrathin CIGS solar cells shows the need to also address recombination losses at the front interface, as well as in the bulk of ultrathin CIGS solar cells. The conjugation of KF-PDT with rear interface passivation is yet to be implemented in ultrathin CIGS solar cells. The application of both treatments may enable the mitigation of front, bulk and rear interface recombination mechanisms, allowing for an enhancement of ultrathin CIGS solar cells electrical properties.

In this work, we present the study of the electrical influence of PDT together with a rear-nano-patterned dielectric layer on ultrathin CIGS solar cell properties. Three type of devices were produced that incorporate different treatments: i) only with KF-PDT; ii) only with rear interface passivation and; iii) with both passivation strategies. Electrical measurements, together with electrical simulations, modelled the effect of PDT and rear interface passivation on the devices optoelectronic properties. Devices with both treatments show a significant enhancement on the electrical properties over devices with only one treatment. Time-Resolved Photoluminescence (TRPL), circuit fitting analysis were used to study the effect of KF-PDT and rear interface passivation on the recombination mechanisms and 1D simulation were performed to understand the impact of these strategies.

Experimental section

An illustrative representation of the fabricated set of devices is shown in Figure 1: i) one with a standard ultrathin CIGS architecture with KF-PDT, named PassKF (Figure 1 a)), ii) one with the addition of an Al_2O_3 dielectric layer, which has no KF-PDT, named $PassAl_2O_3$ (Figure 1 b)), and iii) one with the Al_2O_3 dielectric layer and KF-PDT, named DoublePass (Figure 1 c)). The Al_2O_3 layer was deposited by atomic layer deposition (ALD) with a thickness of 20 nm, directly on top

of the rear contact, Mo. To establish an electrical contact between the CIGS and Mo, the dielectric layer was nano-patterned with point contacts by electron beam lithography followed by an etch step. The point contacts have 200 nm in diameter with a 2 μm pitch (centre to centre) in a quadratic array. The point contacts were opened by reactive ion etching (RIE). A detailed explanation as well as the process conditions for the passivation layer patterning can be found elsewhere.[36,43] Before the CIGS growth, 7 nm of NaF was evaporated on all substrates ensuring Na supply as the out-diffusion from the SLG might be blocked by the passivation layer. [44,45] The CIGS layer was grown using a 3-stage co-evaporation step. The co-evaporation processes needed to be optimized to account for the ultrathin CIGS layer, resulting in a yet to be optimized 3-stage process as the CIGS growth process is highly sensitive to variation in process conditions such as thickness, temperature, pressure, etc.[45] The 3 – stage co-evaporation lead to a small in depth Ga grading that was measured by glow-discharge optical emission spectroscopy, in a standard ultrathin CIGS solar cell. All devices underwent the same CIGS evaporation run with an estimated CIGS thickness of 525 nm and composition values of $[Cu]/([Ga] + [In]) \sim 0.8$ (CGI) and $[Ga]/([Ga] + [In]) \sim 0.3$ (GGI), as measured by X-ray fluorescence (XRF). After the CIGS growth, PassKF and DoublePass underwent KF-PDT treatment. The process was done by spin coating followed at room temperature with a 0.2 Molarity of KF followed by an anneal in N_2 atmosphere at 613.15 K more details in.[42] The substrates were finalized all with the same process conditions, with the final architecture being CIGS/CdS/i-ZnO/ZnO:Al/Ni-Al-Ni[46]. 12 solar cells were made for each type of devices with an area of 0.5 cm^2 defined by mechanical scribing.
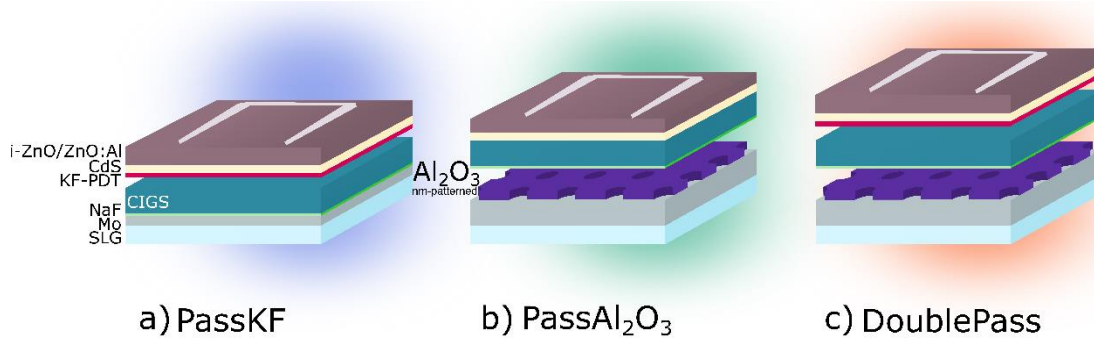
Figure 1 - Illustrative representation of the fabricated devices: a) device with only PDT, PassKF; b) device with only rear interface passivation layer, PassAl$_2$O$_3$; c) device with both treatments, KF-PDT and rear interface passivation, DoublePass. Layers not at scale.

The solar cell current density against voltage (J-V) and the temperature dependent J-V (J-V-T) measurements were conducted in a home-built system with a four-point probe at room temperature. Liquid nitrogen was used as a cooling agent for J-V-T with a measurement being conducted between 100 K and 303.15 K. External quantum efficiency (EQE) measurements were performed on a home-built system. Capacitance-voltage-frequency (C-V-f or C-V) and capacitance–conductance-frequency (C-G-f) measurements were conducted with a precision LCR meter (Agilent E4980 A). The C-V-measurements were taken from -0.6 to 0.8 V with a fixed 10 kHz frequency with a V$_{RMS}$ of 30 mV, at room temperature (RT) in the dark. C-G-f measurements were performed at 0 V bias from 20 Hz to 1 MHz with a V$_{RMS}$ of 30 mV, at RT in the dark. Time-Resolved Photoluminescence (TRPL) was measured at RT with a photospectrometer Picoquant with a TimeHarp 260 single photon counter. The excitation intensity was approximately 0.1 Wcm^{-2}, repetition rate 3 MHz, and excitation wavelength of 532 nm. For simplicity, representative curves of EQE and J-V where chosen based on the averaged values of the individual solar cells in each device. The J_{SC} is corrected to the EQE spectra.

Electrical simulations of the fabricated devices were conducted with SCAPS 1-D software[47], with Table 1 and 2 showing the most important input values, based on measured and literature values.[24,48,49] The CIGS bandgap (E_g) variation was calculated through Eq. 1 based on the Ga profile measured by glow-discharge optical emission spectroscopy[48]:

$$Eg = 1.01 + 0.626 * GGI - 0.167 * GGI * (1 - GGI) \tag{1}$$

From (1), we obtained a small bandgap variation, with an in depth variation of 1.22->1.16->1.22 eV at the front and rear interface, respectively. Since all devices were grown in the same evaporation run, we consider the E_g in depth profile to be similar for all devices. The optical properties of the CIGS layer were measured using an in-house ellipsometry equipment. For the CdS, i-ZnO and ZnO:Al, the optical properties were extracted from the literature[50,51]. The shunt conductance (R_{shunt}) and the series resistance (R_{series}) were extracted from J-V measurements, with the net free carrier concentration (N_{cv}) extracted from C-V measurements.

Table 1 - SCAPS electrical parameters used for the CIGS, CdS, i:ZnO and ZnO:Al layers devices simulations. The CIGS E_g values correspond to the obtained Ga grading. χ_e refers to electron affinity. N_D refers to shallows donors concentration, N_{cv} is the net free carrier concentration.

Parameter	CIGS	CdS	i:ZnO	ZnO:Al
E_g (eV)	1.22->1.16->1.22 (experimental in depth variation)	2.4 [48]	3.3 [48]	3.3 [48]
χ_e (eV)	4.31->4.38->4.301 (experimental in depth variation)	4.11 [48]	4.31 [48]	4.31 [48]
N_D shallow donor (cm^{-3})	10 x 10^1	1 x10^{16} [24,48]	1 x10^{17} [24,48]	1 x10^{20} [24,48]
N_{CV} (cm^{-3})	PassKF:6.05x 10^{15} PassAl$_2$O$_3$: 31.0x 10^{15} DoublePass: 21.0x 10^{15}	0	1 x10^{17} [24]	0

Table 2 – Parameters corresponding to the defects introduced in our model. Defect 1 corresponds to double donor In_{Cu}. N_t corresponds to the correspondent defect concentration, $\sigma_{e/H}$ is the electron and hole capture cross section with E_t being the defect energy, E_{VB} and E_{CB} correspond to the valence band and conduction band energies of the CIGS layer. Defect 2 corresponds to the double acceptor Cu_{In} defect, with Defect 3 being half acceptors and half donors to simulate the electronic activity at the CIGS grain boundaries.

	Type	Distribution	N_t (cm^{-3})	$\sigma_{e/H}$ (cm^2)	E_t
Defect 1 [24,49]	Double Donor	Single	1×10^{13}	$1\times10^{-15}/1\times10^{-13}$	E_{CB}-0.24, E_{CB} -0.34
Defect 2 [24,49]	double acceptor	single	1×10^{13}	$1\times10^{-13}/1\times10^{-15}$	E_{VB}+0.29, E_{VB} + 0.58
Defect 3 [52]	Acceptor/donor		PDT- 5.0×10^{15} No PDT 15×10^{15}	$1\times10^{-15}/1\times10^{-15}$	E_{VB}+0.27

Results

Representative illuminated J-V, dark J-V, and EQE curves are shown in Figure 2 a) and b), respectively. From the J-V curves analysis, we immediately note that the PassKF device shows signs of shunting problems on the illuminated J-V curve. However, the dark J-V curve does not show the same behavior indicating that the device is affected by voltage-dependent current

collection (VDCC)[34,53] and not by shunts. Ultrathin devices without rear passivation often show VDCC due to a high rear interface recombination loss.[34,36] Furthermore, DoublePass device shows a roll-over behavior in the J-V plot leading to a higher series resistance for this device. Roll-over behaviors are caused by several problems usually indicating a back contact barrier.[54,55] The EQE analysis shows a small increase in the 400 - 500 nm range for the devices that underwent the PDT treatment (PassKF and DoublePass) in comparison with PassAl$_2$O$_3$. This enhancement is likely due to a thinner CdS layer for these devices.[7] The devices with the rear passivation (Pass Al$_2$O$_3$ and DoublePass) layer show an increase of the EQE behavior in the wavelength region values between 550 and 1100 nm in comparison with PassKF leading to an increase in the short-circuit current density (J_{SC}) that might be attributed to an increase in the rear optical reflection as well as the passivation properties of Al$_2$O$_3$.[30,35,36] The average figures of merit values obtained from the J-V measurements are summarized in Figure 2 d), as well as the diode quality factor, A, and saturation current density, J_0 — calculated through the dark J-V curves.[56] DoublePass device – with both strategies - shows higher V_{OC} and efficiency values than PassAl$_2$O$_3$ and PassKF. DoublePass V_{OC} values show an increase of 85 mV (abs) over PassKF (604 vs 519 mV, respectively) and 178 mV (abs) over Pass Al$_2$O$_3$ (604 vs 426 mV, respectively) ultimately leading to a 2.2 % and 2.3 % increase in power conversion efficiency values, over PassKF and PassAl$_2$O$_3$ respectively. Despite of lower V_{OC}, PassAl$_2$O$_3$ device shows similar power conversion efficiency value to PassKF (5.6 % vs 5.7 %). So, the impact of individual passivation strategies leads to similar solar cells performance. Despite the enhancement in V_{OC}, the J_{SC} and FF values for DoublePass it does not show a significant increase over PassAl$_2$O$_3$, indicating that the KF-PDT process is not improving carrier collection. The V_{OC} increase by DoublePass indicates a decrease on the impact of the recombination losses, attained by the joint

application of a rear Al_2O_3 passivation layer together with the KF-PDT. In fact, this claim is supported by the saturation current density, J_0, values, as DoublePass shows the lowest J_0, among the fabricated devices. The fact that DoublePass shows the lowest J_0 value is an indication of a reduction of the recombination mechanisms due to the implementation of both strategies. Considering the Shockley-Read-Hall (SRH) recombination model [57,58], the A values of $PassAl_2O_3$, PassKF and DoublePass (2.3 ± 0.5 vs 1.7 ± 0.3 vs 1.3 ± 0.4, respectively) indicates different locations of the dominant recombination mechanism in the active layer: from the space charge region to the quasi neutral region, respectively.[59] From the normalized V_{OC} vs T analysis we extracted the activation energy (E_A) of the saturation current, by performing a linear fit of the V_{OC} in the high temperature range and verifying its value at 0 K.[56] For the studied devices, the E_A value is similar to the bandgap value for DoublePass (1.25 eV) and lower than the bandgap value for PassKF and $PassAl_2O_3$ (0.84 and 0.60 eV, respectively). Additionally, we note that the shunt resistance increases with the application of the dielectric layer. This increase is likely related to a reduction of shunt paths present in the device prevalent in ultrathin CIGS solar cells.[60–62]
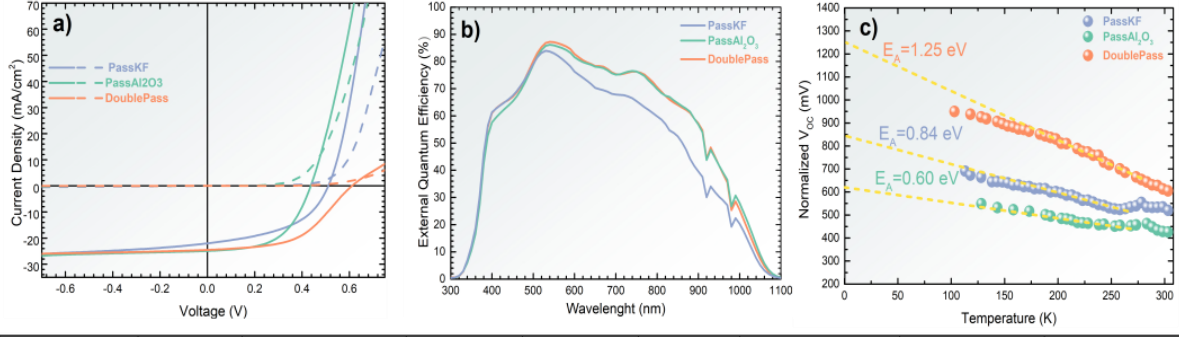
d)	V_{OC} (mV)	J_{SC} (mA/cm^2)	FF (%)	Eff (%)	A	J_0 (mA/cm^2)	R_{shunt} (Ω.cm^2)	R_{Series} (Ω.cm^2)
PassKF	519 ± 45	23.2 ± 1.5	49.0 ± 4.9	5.7 ± 1.6	1.7 ± 0.3	(8.8 ± 0.2) x 10^{-4}	215 ± 70	0.47 ± 0.24
PassAl$_2$O$_3$	426 ± 16	25.4 ± 0.3	51.4 ± 2.6	5.6 ± 0.5	2.3 ± 0.5	(2.9 ± 2.6) x 10^{-2}	495 ± 75	1.27 ± 0.09
DoublePass	604 ± 20	25.5 ± 0.7	51.3 ± 2.4	7.9 ± 0.7	1.3 ± 0.4	(9.1 ± 0.1) x 10^{-5}	617 ± 173	2.96 ± 2.23

Figure 2 – a) Representative dark (dashed) and Illuminated (solid) J-V curves; b) EQE curves for the fabricated devices; c) V_{OC} vs T curves; and d) Averages and standard deviation values of the devices figures of merit for 12 solar cells per device.

C-V measurements were conducted on the studied devices to understand the influence of both passivation strategies on the net free charge carrier concentration (N_{CV}), the CIGS space charge region width (w) as well as in the built-in potential (V_{bi}). treatment.

Table 3 summarizes N_{CV}, w and V_{bi} obtained values, calculated using well-known procedures.[63,64] The devices with the lowest N_{CV} and largest w are the devices with the PDT treatment, PassKF and DoublePass. In the literature, KF-PDT promotes Cd filling of the V_{CU} acceptors, leading to an increase of shallow donors Cd_{Cu} density, so allowing for larger space charge regions and lower values of net free carrier concentration, compatible with trend obtained in our devices.[65] The V_{bi} value of PassKF and DoublePass devices is lower than the measured V_{OC} value. A V_{bi} lower than the V_{OC} may indicate the presence of an electron barrier at the buffer or window layer.[66] The presence of the electron barrier limits the FF value, with little influence

14

on the V_{OC} value.[66] Since, PassKF and DoublePass show V_{bi} values lower than V_{OC}, with similar

FF values, the presence of such electron barrier may be caused by KF-PDT treatment.

Table 3 - N_{CV}, *w* and V_{bi} average and standard deviation values.

Devices	N_{CV} (x 10^{15}cm^{-3})	*w* (nm)	V_{bi} (mV)
PassKF	(6 ± 3)	375 ± 80	453 ± 65
PassAl$_2$O$_3$	(31 ± 6)	167 ± 24	492 ± 61
DoublePass	(21 ± 6)	215 ± 24	548 ± 106

The equivalent circuit fitting analysis of the admittance data allows the study of the device AC response. Hence, we will use the admittance data to perform circuit fitting to identify optoelectronic differences between the studied devices. The impedance data extracted from admittance measurements were fitted using several equivalent circuits through the ZSimpWin 3.50 software.[67] A detailed explanation of the procedure used to consider the most accurate equivalent circuit for each device can be found elsewhere.[68] Figure 3 a),b) and c) shows the equivalent circuit for the fabricated devices with Figure 3d) showing the fitted and estimated parameter for each equivalent circuit. The equivalent circuit for the PassKF device is shown in Figure 3 a) equivalent circuit for PassAl$_2$O$_3$ in Figure 3 b) and the equivalent circuit for DoublePass in Figure 3 c).

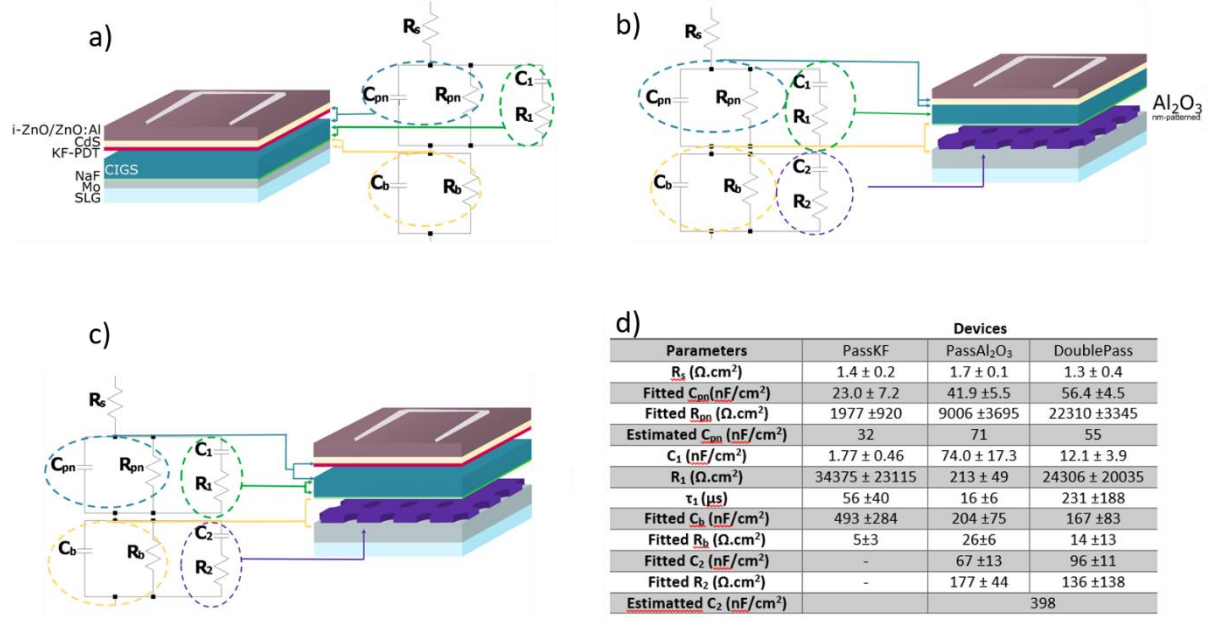| Parameters	Devices		
	PassKF	PassAl$_2$O$_3$	DoublePass
R_s (Ω.cm^2)	1.4 ± 0.2	1.7 ± 0.1	1.3 ± 0.4
Fitted C_{pn} (nF/cm^2)	23.0 ± 7.2	41.9 ±5.5	56.4 ±4.5
Fitted R_{pn} (Ω.cm^2)	1977 ±920	9006 ±3695	22310 ±3345
Estimated C_{pn} (nF/cm^2)	32	71	55
C_1 (nF/cm^2)	1.77 ± 0.46	74.0 ± 17.3	12.1 ± 3.9
R_1 (Ω.cm^2)	34375 ± 23115	213 ± 49	24306 ± 20035
τ_1 (μs)	56 ±40	16 ±6	231 ±188
Fitted C_b (nF/cm^2)	493 ±284	204 ±75	167 ±83
Fitted R_b (Ω.cm^2)	5±3	26±6	14 ±13
Fitted C_2 (nF/cm^2)	-	67 ±13	96 ±11
Fitted R_2 (Ω.cm^2)	-	177 ± 44	136 ±138
Estimatted C_2 (nF/cm^2)		398	

Figure 3-Equivalent electrical circuits for: a) PassKF device; b) PassAl$_2$O$_3$ device, and iii) DoublePass); d) Fitted and estimated parameters average and standard deviation values for the equivalent circuits of all devices.

As shown in Figure 3, each electrical component represents a different type of interface and/or property in the solar cell.[69–72] Rs represents the solar cell series resistance induced by front and rear contacts.[68,70] The depletion region is modelled by C_{pn} and R_{pn} in parallel, representing the p-n junction capacitance and resistance, respectively.[68,73] The rear electrical contact is represented by C_b and R_b in parallel, with C_b being the rear contact capacitance and R_b the rear contact resistance.[70,73] When a C_i capacitance is in series with a resistance R_i it represents a measure anomaly, in the AC regime, that may be associated with a defect trap level.[69,74,75] With i=1,2 being the location in the circuit that corresponds to different anomalies in the assigned device.[64,69] For each C_i-R_i connection in series there is a τ_i representing a characteristic lifetime that for the case of a trap corresponds to the charging/discharging time characteristics of the

associated trap level.[69,74,75] From the fitted circuits, we note that there are two branches with a capacitance in series with a resistance: C_1-R_1 and C_2-R_2. In the literature, C_1-R_1 is associated with defects levels in the absorber layer bulk.[68,76,77] The C_1-R_1 connection is present in all circuits, meaning that in our studied devices, the passivation strategies implemented were not able to mitigate such defect level. The C_2-R_2 is only absent for the device without the Al_2O_3 layer, thus we attribute the C_2-R_2 to a frequency response of the dielectric layer.[68]

The estimated capacitance values were calculated for comparison with the fitted values, in order to validate our results, using the well-known capacitance equation:[78]

$$C = \frac{\varepsilon_0 \varepsilon A}{d} \quad (2)$$

where ε_0 is the vacuum permittivity, ε the dielectric constant, A the solar cell area and d the depletion region width or the Al_2O_3 thickness. The vacuum permittivity has the value of 8.8 x 10-12 F/m; the considered dielectric constant for CIGS is 13.45[79] , and for Al_2O_3 is 9[80]. The fitted C_{pn} values for PassKF (23.0 ± 7.2 nF/cm^2) and DoublePass (56.4 ± 4.5 nF/cm^2) are in good agreement with the calculated ones (32 and 55 respectively), ensuring that the chosen equivalent circuit has physical meaning in this regards. However, the fitted C_{pn} for PassAl$_2$O$_3$ (41.9 ± 5.5 nF/cm^2) device is lower than the estimated one (71 nF/cm^2). Such difference implies the possibility of the CIGS refractive index being changed, something not completely to be discarded due to the extensive known effect of the PDT process. The extracted R_{pn} values for PassAl$_2$O$_3$ and DoublePass increase when compared to PassKF device. The increase of R_{pn} is positive as it reveals that the dielectric layer is effectively mitigating shunts paths that are common in ultrathin CIGS solar cells.[38,60–62] Regarding the C_1-R_1 branch, DoublePass shows a τ_1

value (231 µs) significantly higher than the PassAl$_2$O$_3$ (16 µs), and the PassKF (56 µs). The time constant, τ_1, corresponds to the charge discharge time of a trap level that is the time of capture and emission of an electron.[74] Thus, a higher τ_1 corresponds to a lower recombination velocity. The τ_1 trend suggests that both treatments have a compound effect but also that the impact of KF-PDT mitigates recombination at the absorber bulk since devices with KF-PDT (PassKF and DoublePass) show higher τ_1 value than the device without PDT (PassAl$_2$O$_3$). We observe that C_b values decrease by adding the rear interface passivation layer to the device, indicating that the dielectric introduction is changing the rear contact maybe playing a role in the formation of the MoSe$_2$ layer.[54] Moreover, an increase in R_b values is also observed for PassAl$_2$O$_3$ and DoublePass. Such increase is due to only having 1 % of contacting area at the rear surface, which likely increases contact resistance indicating that the contact pattern needs to be optimized. The presence of C_2-R_2 is due to a response of the nano-patterned dielectric layer to the measurement frequency. We note, that the calculated C_2 capacitance is significantly lower than the estimated C_2 for PassAl$_2$O$_3$ and DoublePass devices. For calculating the Al$_2$O$_3$ capacitance we assumed a conformal non-interrupted layer, which is not the case in the fabricated devices as the Al$_2$O$_3$ covers 99 % of the surface area. Hence, the difference between the estimated and fitted capacitance values of C_2, could be attributed to the nano-patterning of the Al$_2$O$_3$ and to the crystal properties of such thin layer being very different from the ones used for the extraction of the dielectric constant.

The measurements of the carrier lifetime by means of TRPL allow for a better understanding of the impact of the two different passivation strategies in the recombination losses of the studied devices[81–83] and these are shown in are shown in Figure 4. The DoublePass decay is significantly longer than both PassKF and PassAl$_2$O$_3$ devices, which show similar decay curves. The

performed fits considered the deconvolution of the instrumental response. The three TRPL decays follow the same trend, being well described by a biexponential function with two characteristic decay lifetimes: a fast component, often linked to charge separation; and a slower one linked to recombination mechanisms.[84–86] The latter component is the one that allows for insight into the passivation impact on the optoelectronic properties of the devices.[84–86] However, the determination of the factor that defines the TRPL quenching – process that sharply reduces luminescence – is not that straightforward. Since TRPL measurements were carried in final devices, the decay curves can be influenced by different physical factors, including diffusion processes, carrier drift, interface and/or bulk recombination, Ga gradient, among others, which makes the precise determination of the TRPL quenching origin quite puzzling.[83,84] Notwithstanding, the obtained slower lifetime decay values were 0.5 and 0.40 ns for PassKF and PassAl$_2$O$_3$ device, respectively, and 12.6 ns for DoublePass device. It has been shown in CIGS based devices that we are able to correlate recombination mechanisms (lifetime decays) and V$_{OC}$ values.[82,87,88] This correlation suggests the linking between TRPL decay quenching and recombination mechanisms. In fact, from the experimental conditions used it is expected that interface recombination mechanisms have a high impact in the TRPL decay, leading to sharply reduced lifetime decay values, like the ones obtained in PassKF and PassAl$_2$O$_3$ devices. At room temperature the SRH recombination mechanism may be responsible for the TRPL quenching, with deep defects contributing for the TRPL quenching and due to a significant amount of shallow defects contributing for the material conductivity. For PassKF device the ambiguous location for the dominant SRH recombination mechanism, could be located at the space charge region and even at the interface. Nonetheless, TRPL results, in addition to E_A and A values, for the PassKF and PassAl$_2$O$_3$ devices are compatible with interface recombination and again the

combined impact of the two treatments provide for a significant improvement in the DoublePass device.
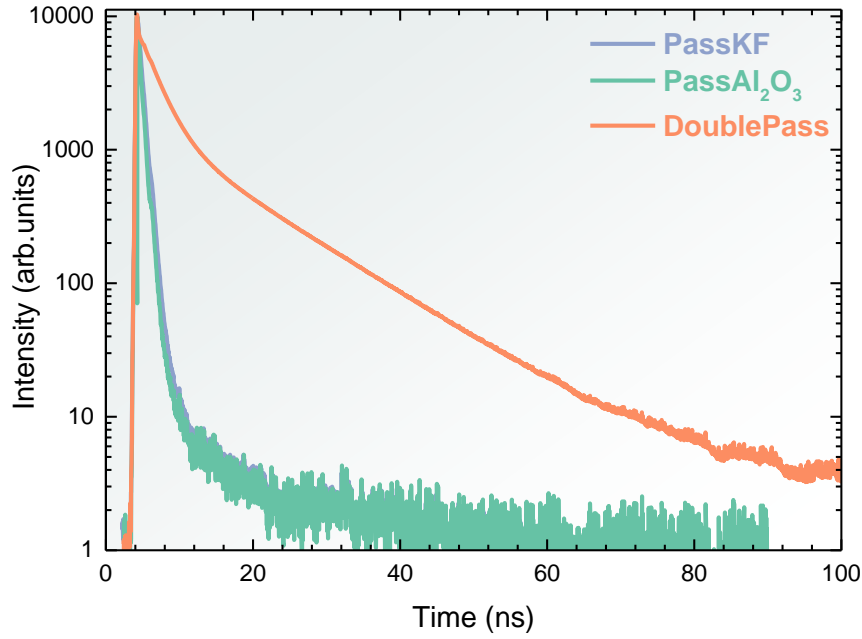

Figure 4 – Normalized TRPL decays at room temperature for all the CIGS studied devices. The decay lifetime was 0.5 ns for PassKF devices, 0.4 ns for PassAl₂O₃ and 12.6 ns for DoublePass device.

To better understand the electrical effects of KF-PDT and rear interface passivation, electrical modelling of the fabricated structures was conducted through SCAPS 1-D simulation. Table shows the simulated J-V figures of merit for the studied devices. The SCAPS baseline model used in this paper was based on parameters used by T.M. Friedlmeier et al.[24], J. Petterson et al.[48], as well as the measured R_{series}, R_{shunt} and N_{CV} values. The modelled effects of PDT were based on the reported effects on the front interface and in the CIGS bulk [7,14,15,52,89]. In particular, we added the following effects related to KF-PDT: i) grain boundary electrical activity by introducing an

defect 270 meV above the valence band with a concentration of 5.0 x 10^{15} cm^{-3} [14,52] and; ii) reducing the acceptor density at the CIGS/CdS interface to simulate the effect of increased donor defects.[15,16,89] To simulate the effect of rear interface passivation, we varied the surface recombination velocity (SRV) value. Since ultrathin CIGS devices have high rear interface recombination, we attributed an SRV of 10^7 cm.s^{-1} for PassKF device and 10^2 cm.s^{-1} for the devices with rear interface passivation, PassAl$_2$O$_3$ and DoublePass according to previous works [30,36]. The rear optical reflection was set at 40 % for PassKF device and 50 % for PassAl$_2$O$_3$ and DoublePass in order to have a good correlation between the simulated and measured J$_{SC}$. The initial simulated *FF* for PassKF and DoublePass device was 15 % and 13.5 % higher than the measured ones, with the PassAl$_2$O$_3$ having a good correlation with the measure value. The R$_{shunt}$ and R$_{series}$ from J-V measurements were taken as an input parameter in order to approach the FF to the measured one for the models. Since only the devices with only KF-PDT show a higher simulated *FF*, the PDT treatment effect may create a barrier at the front interface that lowers FF. In fact, studies report the formation of a K-In-Se$_2$ (KIS) layer[90–92] that was linked to a blocking behaviour.[93] The high bandgap of the KIS layer (2.56 eV) is responsible for the blocking behavior as it increases the conduction band-offset between the CIGS and CdS.[93] In order to verify if our devices have such layer, an extra set of simulations were performed in which we introduced the KIS layer in between the CIGS and CdS and varied its thickness. Figure 5 shows the simulated J-V curves of PassKF device with the addition of the KIS layer. We noticed that just a 5 nm thick KIS layer is sufficient for the FF to drop by 7 %. Further increasing the thickness will leads to small decreases in the *FF* with a roll-over being noticed with a KIS thickness of 50 nm. With the inclusion of a KIS layer in our model the simulated FF for the KF treated devices approached the measured values. The optoelectronic simulations point to a higher

recombination losses in the PassKF and PassAl$_2$O$_3$ devices in comparison to the DoublePass device, in accordance with the experimental results. This higher impact of the recombination losses may be the reason for the higher difference in the V_{OC} values between the simulated and the experimental results for the PassKF and PassAl$_2$O$_3$ devices. For all devices, the simulated J_{SC} values show an excellent correlation with the experimental J_{SC} values. The electrical simulations show that with the introduced KF-PDT, such treatment leads to higher electrical performance than using only rear interface passivation. Regardless of the discrepancies between simulations and the J-V measurements, the electrical simulations show the same electrical trends observed by J-V measurements. This could be an indication that, despite of the slightly different values, the KF-PDT and rear interface passivation effects were correctly modelled as it was the main objective of the simulation, rather than reaching a precise match that is quite complex for cells at this performance stage.

Table 4 - Simulated J-V figures of merit for the studied devices. In brackets, it is represented the variation with the corresponding average experimental J-V parameters for a better comparison.

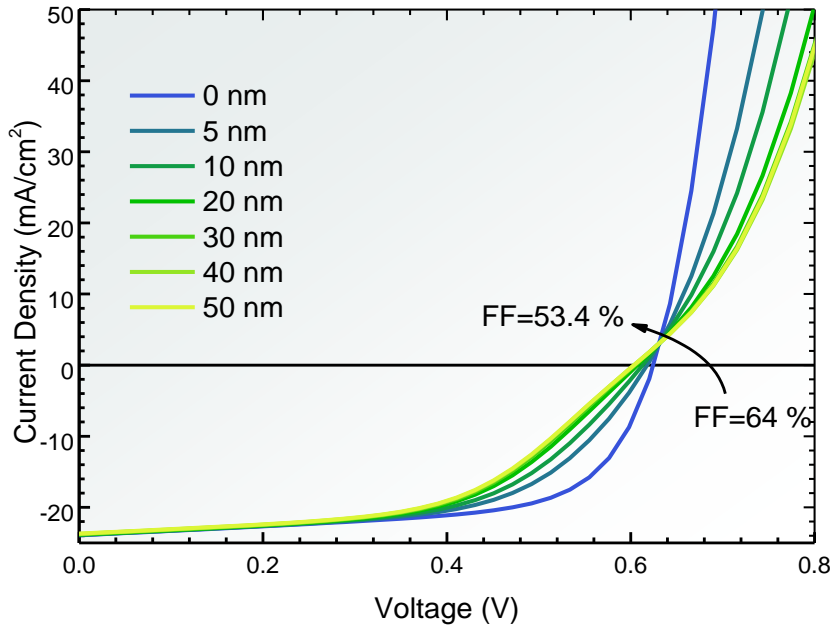| Devices	V$_{OC}$ (mV)	J$_{SC}$ (mA/cm^2)	FF (%)	Eff (%)
PassKF	617 (+98)	23.9 (+0.7)	57.8 (+6.5)	8.5 (+2.8)
PassAl$_2$O$_3$	612 (+186)	25.1 (-0.3)	54.3 (+2.9)	8.3 (+2.7)
DoublePass	657 (+53)	25.4 (-0.1)	58.8 (+ 7.5)	9.7 (+1.8)

Figure 5 – J-V curves of PassKF device with a thickness variation of the KIS layer. The thickness range from 0 to 50 nm. The *FF* difference between no KIS and a KIS layer 50 nm thick is shown.

DISCUSSION

We report, for the first time, the implementation of a KF-PDT treatment together with a rear interface passivation scheme in ultrathin CIGS solar cells. Moreover, we show that only the application of both treatments the maximum potential of a solar cell is revealed as, individually, each of the improvements is not enough to counter for all the dominant losses. J-V measurements shows that the DoublePass device - with both passivation strategies - has the highest V_{OC} value of 604 mV, which translates into the device with the highest efficiency value of this study, 7.9 %. However, DoublePass device shows the presence of a roll-over in the J-V behavior, common

in devices with insufficient Sodium (Na) as the passivation layer acts as a Na diffusion barrier [44,94]. However, since all devices had a pre-deposition of 7 nm of NaF and only DoublePass shows the roll-over and, SCAPS simulation hinted at the presence of a blocking layer at the front interface, the roll-over anomaly could be due to the conjugation of the dielectric blocking Na diffusion and a possible presence of a KIS layer at the front interface. Figure 6 shows the difference between the measured and simulated figures of merit for the fabricated devices. From the figure, the simulated FF for PassKF and DoublePass could only be approximated by the J-V measured values with the inclusion of a KIS layer at the front interface. Such layer is linked with a blocking behavior as it causes a higher conduction band offset between CIGS and CdS.[93] With the inclusion of a KIS layer in our model, the simulated FF approached the measured value, for the KF-treated devices. In fact, the presence of a blocking layer is also hinted by the V_{bi} values extracted from the C-V measurements, which were lower than the measured V_{OC} values for the KF-treated devices. Thus, it might be possible that the PDT devices have a KIS layer and it should be responsible for the low FF values as well as the V_{bi} values lower than V_{OC}. [66] The V_{OC} value of the DoublePass device is the highest among the studied devices and the J_0 value is the lowest, suggesting that several recombination mechanisms are mitigated compared to the other studied devices, which is supported by the highest charge carrier's lifetime value observed in TRPL. The E_A value gives information of what is the type of dominant Shockley-Read-Hall (SRH) recombination[56–58]: if $E_A \sim E_g$, the dominant recombination mechanism is present in the CIGS bulk; and if $E_A < E_g$, then an interface issue is detected. For DoublePass device, the electrical and optoelectronic results, E_A (1.25 eV), A value (1.3) and longer TRPL decay time, support a dominant SRH recombination in the absorber bulk. For the other studied devices, the E_A value is lower than the bandgap value (0.84 eV for PassKF and 0.60 eV for PassAl$_2$O$_3$). The

E_A values together with A values indicate that for PassKF and PassAl$_2$O$_3$ devices bulk recombination is not the dominant mechanism.[56] TRPL measurements show a significant increase in the carrier lifetime from DoublePass with regards to PassKF and PassAl$_2$O$_3$, with these last two devices showing very similar carrier lifetimes. Moreover, from PassKF to PassAl$_2$O$_3$ device, we observe an increase of 18 % in the decay lifetime, which is surprisingly the same increase observed in the V_{OC} value. So, these results suggest that the implementation of both passivation strategies were able to neutralize dominant interface recombination mechanisms present in PassKF and PassAl$_2$O$_3$. Nonetheless, the circuit fitting analysis points out that the DoublePass device has the highest τ_1 value, suggesting that even the bulk recombination is somehow mitigated compared to the other studied devices. The A value of PassAl$_2$O$_3$ may be not explained by SRH recombination mechanism, since A values higher than 2 are not described by the SRH model[95] and need to be described by other recombination mechanisms such as fluctuating potentials or tunneling effect.[95,96] Electrical and optoelectronic results suggest that rear interface recombination in the devices is ineffective when front interface or bulk recombination values are very high and dominant. By linking the decay lifetime with recombination in the devices [82,84,87], the TRPL measurements suggest that from the low carrier lifetime of PassKF and PassAl$_2$O$_3$ devices, that front interface recombination is the dominant recombination mechanism on these devices, which is also suggested by the E_A and A values obtained in the J-V analysis.

All in all, we show that, in order to have proper rear interface passivation gains, the CIGS/CdS interface and the bulk quality of CIGS must be treated, otherwise a rear interface passivation strategy does not lead to optoelectronic gains as other losses would still be dominant. The measurements performed in this study showed that KF-PDT together with rear interface

passivation, reduces recombination at the rear interface, at the front interface and that improves the bulk region. Both strategies must be coupled together to minimize recombination losses, thus maximizing the electrical performance of ultrathin CIGS solar cells.
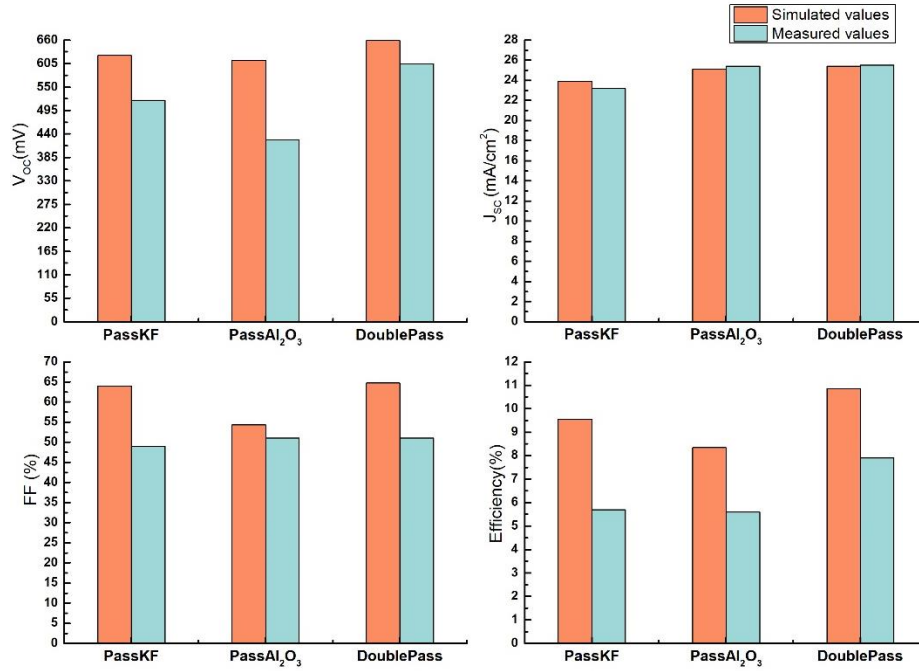

Figure 6 - Comparison between the simulated and measured solar cells figures of merit.

Conclusion

A Rear interface passivation strategy and a post-deposition treatment were for the first time applied at the same time in ultrathin CIGS solar cells. Rear interface passivation was achieved with the introduction of a 20 nm nano-patterned Al_2O_3 layer with the PDT being performed with KF. From the measurements performed, we conclude that, in order to have significant optolectronic gains all the recombination mechanisms must be dealt with. The implementation of both strategies leads to significant enhancements of the optoelectronic properties. Despite of the

observed improvement, the presence of the roll-over for DoublePass indicates room for further improvements in the KF-PDT deposition conditions as well as how NaF is introduced with a blocking-dielectric layer. And these findings are corroborated be electrical 1-D simulation. The decay time of the studied devices was profoundly affected by front interface recombination, as PassKF and PassAl$_2$O$_3$ devices show quite low decay times. However, DoublePass showed a significant higher lifetime value over the devices with only one treatment, suggesting the positive of using both strategies. Admittance circuit fitting analysis showed the presence of active recombination channels in the absorber bulk and that KF-PDT is able to reduce its impact. Altogether, our striking results suggest the need to address losses at the front surface and bulk to successfully implement rear interface passivation and that both strategies need to be used in tandem as no silver bullet exist to provide ultrathin solar cells with an unique solution to its drawbacks.

Corresponding Author

Corresponding Author:

Email: tomas.lopes@inl.int

Author Contributions

The manuscript was written through contributions of all authors. All authors have given approval to the final version of the manuscript.

Acknowledgements

References

(1) Chen, W. S.; Stewart, J. M.; Stanbery, B. J.; Devaney, W. E.; Mickelsen, R. A. Development of Thin Film Polycrystalline $CuIn_{1-x}Ga_xSe_2$ Solar Cells. In *Photovoltaic specialists conference. 19*; 1987; pp 1445–1447.

(2)   Potter, R. R. Enhanced Photocurrent ZnO/CdS/CuInSe$_2$ Solar Cells. *Solar Cells* **1986**, *16*, 521–527. https://doi.org/10.1016/0379-6787(86)90107-9.

(3)   Hedstrom, J.; Ohlsen, H.; Bodegard, M.; Kylner, A.; Stolt, L.; Hariskos, D.; Ruckh, M.; Schock, H.-W. ZnO/CdS/Cu(In,Ga)Se$_2$ Thin Film Solar Cells with Improved Performance. In *Conference Record of the Twenty Third IEEE Photovoltaic Specialists Conference - 1993 (Cat. No.93CH3283-9)*; 1993; pp 364–371. https://doi.org/10.1109/PVSC.1993.347154.

(4)   Contreras, M. A.; Ramanathan, K.; AbuShama, J.; Hasoon, F.; Young, D. L.; Egaas, B.; Noufi, R. SHORT COMMUNICATION: ACCELERATED PUBLICATION: Diode Characteristics in State-of-the-Art ZnO/CdS/Cu(In$_{1-x}$Ga$_x$)Se$_2$ Solar Cells. *Progress in Photovoltaics: Research and Applications* **2005**, *13* (3), 209–216. https://doi.org/10.1002/pip.626.

(5)   Rau, U.; Jasenek, A.; Schock, H. W.; Engelhardt, F.; Meyer, T. Electronic Loss Mechanisms in Chalcopyrite Based Heterojunction Solar Cells. *Thin Solid Films* **2000**, *361–362*, 298–302. https://doi.org/10.1016/S0040-6090(99)00762-2.

(6)   Gloeckler, M.; Sites, J. R. Efficiency Limitations for Wide-Band-Gap Chalcopyrite Solar Cells. *Thin Solid Films* **2005**, *480–481*, 241–245. https://doi.org/10.1016/j.tsf.2004.11.018.

(7)   Chirilă, A.; Reinhard, P.; Pianezzi, F.; Bloesch, P.; Uhl, A. R.; Fella, C.; Kranz, L.; Keller, D.; Gretener, C.; Hagendorfer, H.; Jaeger, D.; Erni, R.; Nishiwaki, S.; Buecheler, S.; Tiwari, A. N. Potassium-Induced Surface Modification of Cu(In,Ga)Se$_2$ Thin Films for High-Efficiency Solar Cells. *Nature Materials* **2013**, *12* (12), 1107–1111. https://doi.org/10.1038/nmat3789.

(8)   Jackson, P.; Hariskos, D.; Wuerz, R.; Kiowski, O.; Bauer, A.; Friedlmeier, T. M.; Powalla, M. Properties of Cu(In,Ga)Se $_2$ Solar Cells with New Record Efficiencies up to 21.7%: Properties of Cu(In,Ga)Se $_2$ Solar Cells with New Record Efficiencies up to 21.7%. *Phys. Status Solidi RRL* **2015**, *9* (1), 28–31. https://doi.org/10.1002/pssr.201409520.

(9)   Jackson, P.; Hariskos, D.; Wuerz, R.; Wischmann, W.; Powalla, M. Compositional Investigation of Potassium Doped Cu(In,Ga)Se $_2$ Solar Cells with Efficiencies up to 20.8%: Compositional Investigation of Potassium Doped Cu(In,Ga)Se $_2$ Solar Cells with Efficiencies up to 20.8%. *Phys. Status Solidi RRL* **2014**, *8* (3), 219–222. https://doi.org/10.1002/pssr.201409040.

(10) Kamada, R.; Yagioka, T.; Adachi, S.; Handa, A.; Tai, K. F.; Kato, T.; Sugimoto, H. New World Record Cu(In, Ga)(Se, S)$_2$ Thin Film Solar Cell Efficiency beyond 22%. In *2016 IEEE 43rd Photovoltaic Specialists Conference (PVSC)*; 2016; pp 1287–1291. https://doi.org/10.1109/PVSC.2016.7749822.

(11) Jackson, P.; Wuerz, R.; Hariskos, D.; Lotter, E.; Witte, W.; Powalla, M. Effects of Heavy Alkali Elements in Cu(In,Ga)Se$_2$ Solar Cells with Efficiencies up to 22.6%. *physica status solidi (RRL) – Rapid Research Letters* **2016**, *10* (8), 583–586. https://doi.org/10.1002/pssr.201600199.

(12) Kato, T.; Wu, J.-L.; Hirai, Y.; Sugimoto, H.; Bermudez, V. Record Efficiency for Thin-Film Polycrystalline Solar Cells Up to 22.9% Achieved by Cs-Treated Cu(In,Ga)(Se,S)$_2$. *IEEE Journal of Photovoltaics* **2019**, *9* (1), 325–330. https://doi.org/10.1109/JPHOTOV.2018.2882206.

(13) Kanevce, A.; Paetel, S.; Hariskos, D.; Magorian Friedlmeier, T. Impact of RbF-PDT on Cu(In,Ga)Se $_2$ Solar Cells with CdS and Zn(O,S) Buffer Layers. *EPJ Photovolt.* **2020**, *11*, 8. https://doi.org/10.1051/epjpv/2020005.

(14) Siebentritt, S.; Avancini, E.; Bär, M.; Bombsch, J.; Bourgeois, E.; Buecheler, S.; Carron, R.; Castro, C.; Duguay, S.; Félix, R.; Handick, E.; Hariskos, D.; Havu, V.; Jackson, P.; Komsa, H.; Kunze, T.; Malitckaya, M.; Menozzi, R.; Nesladek, M.; Nicoara, N.; Puska, M.; Raghuwanshi, M.; Pareige, P.; Sadewasser, S.; Sozzi, G.; Tiwari, A. N.; Ueda, S.; Vilalta-Clemente, A.; Weiss, T. P.; Werner, F.; Wilks, R. G.; Witte, W.; Wolter, M. H. Heavy Alkali Treatment of Cu(In,Ga)Se $_2$ Solar Cells: Surface versus Bulk Effects. *Adv. Energy Mater.* **2020**, *10* (8), 1903752. https://doi.org/10.1002/aenm.201903752.

(15) Pianezzi, F.; Reinhard, P.; Chirilă, A.; Bissig, B.; Nishiwaki, S.; Buecheler, S.; Tiwari, A. N. Unveiling the Effects of Post-Deposition Treatment with Different Alkaline Elements on the Electronic Properties of CIGS Thin Film Solar Cells. *Phys. Chem. Chem. Phys.* **2014**, *16* (19), 8843. https://doi.org/10.1039/c4cp00614c.

(16) Aguiar, J. A.; Stokes, A.; Jiang, C.-S.; Aoki, T.; Kotula, P. G.; Patel, M. K.; Gorman, B.; Al-Jassim, M. Revealing Surface Modifications of Potassium-Fluoride-Treated Cu(In,Ga)Se$_2$: A Study of Material Structure, Chemistry, and Photovoltaic Performance. *Advanced Materials Interfaces* **2016**, *3* (17), 1600013. https://doi.org/10.1002/admi.201600013.

(17) Muzzillo, C. P.; Poplawsky, J. D.; Tong, H. M.; Guo, W.; Anderson, T. Revealing the Beneficial Role of K in Grain Interiors, Grain Boundaries, and at the Buffer Interface for Highly Efficient CuInSe$_2$ Solar Cells. *Progress in Photovoltaics: Research and Applications* **2018**, *26* (10), 825–834. https://doi.org/10.1002/pip.3022.

(18) Handick, E.; Reinhard, P.; Alsmeier, J.-H.; Köhler, L.; Pianezzi, F.; Krause, S.; Gorgoi, M.; Ikenaga, E.; Koch, N.; Wilks, R. G.; Buecheler, S.; Tiwari, A. N.; Bär, M. Potassium Postdeposition Treatment-Induced Band Gap Widening at Cu(In,Ga)Se$_2$ Surfaces – Reason for

Performance Leap? *ACS Appl. Mater. Interfaces* **2015**, *7* (49), 27414–27420. https://doi.org/10.1021/acsami.5b09231.

(19) Schöppe, P.; Schönherr, S.; Jackson, P.; Wuerz, R.; Wisniewski, W.; Ritzer, M.; Zapf, M.; Johannes, A.; Schnohr, C. S.; Ronning, C. Overall Distribution of Rubidium in Highly Efficient Cu(In,Ga)Se$_2$ Solar Cells. *ACS Appl. Mater. Interfaces* **2018**, *10* (47), 40592–40598. https://doi.org/10.1021/acsami.8b16040.

(20) de Wild, J.; Buldu, D. G.; Schnabel, T.; Simor, M.; Kohl, T.; Birant, G.; Brammertz, G.; Meuris, M.; Poortmans, J.; Vermang, B. High Voc upon KF Post-Deposition Treatment for Ultrathin Single-Stage Coevaporated Cu(In, Ga)Se$_2$ Solar Cells. *ACS Appl. Energy Mater.* **2019**, *2* (8), 6102–6111. https://doi.org/10.1021/acsaem.9b01370.

(21) Jensen, S. A.; Glynn, S.; Kanevce, A.; Dippo, P.; Li, J. V.; Levi, D. H.; Kuciauskas, D. Beneficial Effect of Post-Deposition Treatment in High-Efficiency Cu(In,Ga)Se$_2$ Solar Cells through Reduced Potential Fluctuations. *J. Appl. Phys.* **2016**, *120* (6), 063106. https://doi.org/10.1063/1.4960344.

(22) Sun, Y.; Lin, S.; Li, W.; Cheng, S.; Zhang, Y.; Liu, Y.; Liu, W. Review on Alkali Element Doping in Cu(In,Ga)Se$_2$ Thin Films and Solar Cells. *Engineering* **2017**, *3* (4), 452–459. https://doi.org/10.1016/J.ENG.2017.04.020.

(23) Kiss, J.; Gruhn, T.; Roma, G.; Felser, C. Theoretical Study on the Structure and Energetics of Cd Insertion and Cu Depletion of CuIn$_5$Se$_8$. *J. Phys. Chem. C* **2013**, *117* (21), 10892–10900. https://doi.org/10.1021/jp312467f.

(24) Friedlmeier, T. M.; Jackson, P.; Bauer, A.; Hariskos, D.; Kiowski, O.; Wuerz, R.; Powalla, M. Improved Photocurrent in Cu(In,Ga)Se$_2$ Solar Cells: From 20.8% to 21.7% Efficiency with CdS Buffer and 21.0% Cd-Free. *IEEE J. Photovoltaics* **2015**, *5* (5), 1487–1491. https://doi.org/10.1109/JPHOTOV.2015.2458039.

(25) Kohl, T.; Rivas, N. A.; de Wild, J.; Buldu, D. G.; Birant, G.; Brammertz, G.; Meuris, M.; Renner, F. U.; Poortmans, J.; Vermang, B. Inclusion of Water in Cu(In, Ga)Se$_2$ Absorber Material During Accelerated Lifetime Testing. *ACS Appl. Energy Mater.* **2020**, *3* (6), 5120–5125. https://doi.org/10.1021/acsaem.0c00610.

(26) Fthenakis, V. Sustainability of Photovoltaics: The Case for Thin-Film Solar Cells. *Renewable and Sustainable Energy Reviews* **2009**, *13* (9), 2746–2750.

(27) Gloeckler, M.; Sites, J. R. Potential of Submicrometer Thickness Cu(In,Ga)Se$_2$ Solar Cells. *Journal of Applied Physics* **2005**, *98* (10), 103703. https://doi.org/10.1063/1.2128054.

(28) Amin, N.; Chelvanathan, P.; Hossain, M. I.; Sopian, K. Numerical Modelling of Ultra Thin Cu(In,Ga)Se2 Solar Cells. *Energy Procedia* **2012**, *15*, 291–298. https://doi.org/10.1016/j.egypro.2012.02.034.

(29) Han, A.; Zhang, Y.; Song, W.; Li, B.; Liu, W.; Sun, Y. Structure, Morphology and Properties of Thinned Cu(In, Ga)Se$_2$ Films and Solar Cells. *Semicond. Sci. Technol.* **2012**, *27* (3), 035022. https://doi.org/10.1088/0268-1242/27/3/035022.

(30) Vermang, B.; Fjällström, V.; Pettersson, J.; Salomé, P.; Edoff, M. Development of Rear Surface Passivated Cu(In,Ga)Se$_2$ Thin Film Solar Cells with Nano-Sized Local Rear Point

Contacts. *Solar Energy Materials and Solar Cells* **2013**, *117*, 505–511. https://doi.org/10.1016/j.solmat.2013.07.025.

(31) Kotipalli, R.; Delamare, R.; Poncelet, O.; Tang, X.; Francis, L. A.; Flandre, D. Passivation Effects of Atomic-Layer-Deposited Aluminum Oxide. *EPJ Photovolt.* **2013**, *4*, 45107. https://doi.org/10.1051/epjpv/2013023.

(32) Aberle, A. G.; Glunz, S.; Warta, W. Impact of Illumination Level and Oxide Parameters on Shockley–Read–Hall Recombination at the Si-SiO$_2$ Interface. *Journal of Applied Physics* **1992**, *71* (9), 4422–4431. https://doi.org/10.1063/1.350782.

(33) Dingemans, G.; Kessels, W. M. M. Status and Prospects of Al$_2$O$_3$ -Based Surface Passivation Schemes for Silicon Solar Cells. *Journal of Vacuum Science & Technology A: Vacuum, Surfaces, and Films* **2012**, *30* (4), 040802. https://doi.org/10.1116/1.4728205.

(34) Salomé, P. M. P.; Vermang, B.; Ribeiro-Andrade, R.; Teixeira, J. P.; Cunha, J. M. V.; Mendes, M. J.; Haque, S.; Borme, J.; Águas, H.; Fortunato, E.; Martins, R.; González, J. C.; Leitão, J. P.; Fernandes, P. A.; Edoff, M.; Sadewasser, S. Passivation of Interfaces in Thin Film Solar Cells: Understanding the Effects of a Nanostructured Rear Point Contact Layer. *Adv. Mater. Interfaces* **2018**, *5* (2), 1701101. https://doi.org/10.1002/admi.201701101.

(35) Vermang, B.; Watjen, J. T.; Frisk, C.; Fjallstrom, V.; Rostvall, F.; Edoff, M.; Salome, P.; Borme, J.; Nicoara, N.; Sadewasser, S. Introduction of Si PERC Rear Contacting Design to Boost Efficiency of Cu(In,Ga)Se $_2$ Solar Cells. *IEEE J. Photovoltaics* **2014**, *4* (6), 1644–1649. https://doi.org/10.1109/JPHOTOV.2014.2350696.

(36) Bose, S.; Cunha, J. M. V.; Borme, J.; Chen, W. C.; Nilsson, N. S.; Teixeira, J. P.; Gaspar, J.; Leitão, J. P.; Edoff, M.; Fernandes, P. A.; Salomé, P. M. P. A Morphological and Electronic Study of Ultrathin Rear Passivated Cu(In,Ga)Se$_2$ Solar Cells. *Thin Solid Films* **2019**, *671*, 77–84. https://doi.org/10.1016/j.tsf.2018.12.028.

(37) Cunha, J. M. V.; Fernandes, P. A.; Salome, P. M. P.; Lopes, T. S.; Bose, S.; Hultqvist, A.; Chen, W.-C.; Donzel-Gargand, O.; Ribeiro, R. M.; Oliveira, A. J. N.; Edoff, M. Decoupling of Optical and Electrical Properties of Rear Contact CIGS Solar Cells. *IEEE J. Photovoltaics* **2019**, *9* (6), 1857–1862. https://doi.org/10.1109/JPHOTOV.2019.2933357.

(38) Lopes, T. S.; Cunha, J. M. V.; Bose, S.; Barbosa, J. R. S.; Borme, J.; Donzel-Gargand, O.; Rocha, C.; Silva, R.; Hultqvist, A.; Chen, W.-C.; Silva, A. G.; Edoff, M.; Fernandes, P. A.; Salome, P. M. P. Rear Optical Reflection and Passivation Using a Nanopatterned Metal/Dielectric Structure in Thin-Film Solar Cells. *IEEE J. Photovoltaics* **2019**, *9* (5), 1421–1427. https://doi.org/10.1109/JPHOTOV.2019.2922323.

(39) Bose, S.; Cunha, J. M. V.; Suresh, S.; De Wild, J.; Lopes, T. S.; Barbosa, J. R. S.; Silva, R.; Borme, J.; Fernandes, P. A.; Vermang, B.; Salomé, P. M. P. Optical Lithography Patterning of SiO$_2$ Layers for Interface Passivation of Thin Film Solar Cells. *Sol. RRL* **2018**, *2* (12), 1800212. https://doi.org/10.1002/solr.201800212.

(40) Mollica, F.; Goffard, J.; Jubault, M.; Donsanti, F.; Collin, S.; Cattoni, A.; Lombez, L.; Naghavi, N. Comparative Study of Patterned TiO$_2$ and Al$_2$O$_3$ Layers as Passivated Back-Contact for Ultra-Thin Cu(In, Ga)Se$_2$ Solar Cells. In *2016 IEEE 43rd Photovoltaic Specialists Conference (PVSC)*; 2016; pp 2213–2217. https://doi.org/10.1109/PVSC.2016.7750028.

(41) Casper, P.; Hünig, R.; Gomard, G.; Kiowski, O.; Reitz, C.; Lemmer, U.; Powalla, M.; Hetterich, M. Optoelectrical Improvement of Ultra-Thin Cu(In,Ga)Se $_2$ Solar Cells through Microstructured MgF $_2$ and Al $_2$ O $_3$ Back Contact Passivation Layer. *Phys. Status Solidi RRL* **2016**, *10* (5), 376–380. https://doi.org/10.1002/pssr.201600018.

(42) de Wild, J.; Kohl, T.; Buldu, D. G.; Birant, G.; Parragh, D. M.; Brammertz, G.; Meuris, M.; Poortmans, J.; Vermang, B. KF Postdeposition Treatment in N_2 of Single-Stage Thin Cu(In,Ga)Se$_2$ Absorber Layers. *IEEE Journal of Photovoltaics* **2020**, *10* (1), 255–258. https://doi.org/10.1109/JPHOTOV.2019.2947758.

(43) Vermang, B.; Ren, Y.; Joel, J.; Frisk, C.; Donzel-Gargand, O.; Salomé, P.; Borme, J.; Sadewasser, S.; Platzer-Björkman, C.; Edoff, M. Rear Surface Optimization of CZTS Solar Cells by Use of a Passivation Layer with Nano-Sized Point Openings. In *2015 IEEE 42nd Photovoltaic Specialist Conference (PVSC)*; 2015; pp 1–3. https://doi.org/10.1109/PVSC.2015.7355624.

(44) Salomé, P.; Fjällström, V.; Hultqvist, A.; Edoff, M. Na Doping of CIGS Solar Cells Using Low Sodium-Doped Mo Layer. *IEEE Journal of Photovoltaics* **2013**, *3* (1), 509–513. https://doi.org/10.1109/JPHOTOV.2012.2226144.

(45) Salomé, P. M. P.; Hultqvist, A.; Fjällström, V.; Edoff, M.; Aitken, B. G.; Zhang, K.; Fuller, K.; Kosik Williams, C. Incorporation of Na in Cu(In,Ga)Se$_2$ Thin-Film Solar Cells: A Statistical Comparison Between Na From Soda-Lime Glass and From a Precursor Layer of NaF. *IEEE Journal of Photovoltaics* **2014**, *4* (6), 1659–1664. https://doi.org/10.1109/JPHOTOV.2014.2357261.

(46) Garud, S.; Gampa, N.; Allen, T. G.; Kotipalli, R.; Flandre, D.; Batuk, M.; Hadermann, J.; Meuris, M.; Poortmans, J.; Smets, A.; Vermang, B. Surface Passivation of CIGS Solar Cells Using Gallium Oxide. *Phys. Status Solidi A* **2018**, *215* (7), 1700826. https://doi.org/10.1002/pssa.201700826.

(47) Burgelman, M.; Nollet, P.; Degrave, S. Modelling Polycrystalline Semiconductor Solar Cells. *Thin Solid Films* **2000**, *361–362*, 527–532. https://doi.org/10.1016/S0040-6090(99)00825-1.

(48) Pettersson, J.; Platzer-Björkman, C.; Zimmermann, U.; Edoff, M. Baseline Model of Graded-Absorber $Cu(In,Ga)Se_2$ Solar Cells Applied to Cells with $Zn_{1-x}Mg_xO$ Buffer Layers. *Thin Solid Films* **2011**, *519* (21), 7476–7480. https://doi.org/10.1016/j.tsf.2010.12.141.

(49) Rincon, C.; Marquez, R. Defect Physics of the $CuInSe_2$ Chalcopyrite Semiconductor. *Journal of Physics and Chemistry of Solids* **1999**, 9.

(50) Carron, R.; Avancini, E.; Feurer, T.; Bissig, B.; Losio, P. A.; Figi, R.; Schreiner, C.; Bürki, M.; Bourgeois, E.; Remes, Z.; Nesladek, M.; Buecheler, S.; Tiwari, A. N. Refractive Indices of Layers and Optical Simulations of $Cu(In,Ga)Se_2$ Solar Cells. *Sci Technol Adv Mater* **2018**, *19* (1), 396–410. https://doi.org/10.1080/14686996.2018.1458579.

(51) Werner, W. S. M.; Glantschnig, K.; Ambrosch-Draxl, C. Optical Constants and Inelastic Electron-Scattering Data for 17 Elemental Metals. *Journal of Physical and Chemical Reference Data* **2009**, *38* (4), 1013–1092. https://doi.org/10.1063/1.3243762.

(52)   Taretto, K.; Rau, U. Numerical Simulation of Carrier Collection and Recombination at Grain Boundaries in Cu(In,Ga)Se$_2$ Solar Cells. *Journal of Applied Physics* **2008**, *103* (9), 094523. https://doi.org/10.1063/1.2917293.

(53)   Photovoltaic Properties of Standard Devices. In *Chalcogenide Photovoltaics*; John Wiley & Sons, Ltd, 2011; pp 277–304. https://doi.org/10.1002/9783527633708.ch6.

(54)   Salomé, P. M. P.; Fjallstrom, V.; Hultqvist, A.; Szaniawski, P.; Zimmermann, U.; Edoff, M. The Effect of Mo Back Contact Ageing on Cu(In,Ga)Se$_2$ Thin-Film Solar Cells. *Progress in Photovoltaics: Research and Applications* **2014**, *22* (1), 83–89. https://doi.org/10.1002/pip.2360.

(55)   Umehara, T.; Nakada, K.; Yamada, A. Impact of Roll-over-Shaped Current–Voltage Characteristics and Device Properties of Ag(In,Ga)Se2 Solar Cells. *Jpn. J. Appl. Phys.* **2016**, *56* (1), 012302. https://doi.org/10.7567/JJAP.56.012302.

(56)   Hegedus, S. S.; Shafarman, W. N. Thin-Film Solar Cells: Device Measurements and Analysis. *Progress in Photovoltaics: Research and Applications* **2004**, *12* (2–3), 155–176. https://doi.org/10.1002/pip.518.

(57)   Shockley, W.; Read, W. T. Statistics of the Recombinations of Holes and Electrons. *Phys. Rev.* **1952**, *87* (5), 835–842. https://doi.org/10.1103/PhysRev.87.835.

(58)   Hall, R. N. Electron-Hole Recombination in Germanium. *Phys. Rev.* **1952**, *87* (2), 387–387. https://doi.org/10.1103/PhysRev.87.387.

(59)   Scheer, R. Towards an Electronic Model for CuIn$_{1-x}$Ga$_x$Se$_2$ Solar Cells. *Thin Solid Films* **2011**, *519* (21), 7472–7475. https://doi.org/10.1016/j.tsf.2011.01.092.

(60) Lundberg, O.; Bodegård, M.; Malmström, J.; Stolt, L. Influence of the Cu(In,Ga)Se$_2$ Thickness and Ga Grading on Solar Cell Performance. *Progress in Photovoltaics: Research and Applications* **2003**, *11* (2), 77–88. https://doi.org/10.1002/pip.462.

(61) Duchatelet, A.; Letty, E.; Jaime-Ferrer, S.; Grand, P.-P.; Mollica, F.; Naghavi, N. The Impact of Reducing the Thickness of Electrodeposited Stacked Cu/In/Ga Layers on the Performance of CIGS Solar Cells. *Solar Energy Materials and Solar Cells* **2017**, *162*, 114–119. https://doi.org/10.1016/j.solmat.2016.12.045.

(62) Sharaman, W. N.; Birkmire, R. W.; Marsillac, S.; Marudachalam, M.; Orbey, N.; Russell, T. W. F. Effect of Reduced Deposition Temperature, Time, and Thickness on Cu(InGa)Se$_2$ Films and Devices. In *Conference Record of the Twenty Sixth IEEE Photovoltaic Specialists Conference - 1997*; 1997; pp 331–334. https://doi.org/10.1109/PVSC.1997.654095.

(63) Hilibrand, J.; Gold, R. Determination of the Impurity Distribution in Junction Diodes from Capacitance-Voltage Measurements. *RCA review* **1960**, *21* (2), 245–252.

(64) P-n Junctions. In *Physics of Semiconductor Devices*; John Wiley & Sons, Ltd, 2006; pp 77–133. https://doi.org/10.1002/9780470068328.ch2.

(65) Persson, C.; Zhao, Y.-J.; Lany, S.; Zunger, A. N -Type Doping of CuInSe$_2$ and CuGaSe$_2$. *Phys. Rev. B* **2005**, *72* (3), 035211. https://doi.org/10.1103/PhysRevB.72.035211.

(66) Kron, G.; Egerter, T.; Werner, J. H.; Rau, U. Electronic Transport in Dye-Sensitized Nanoporous TiO$_2$ Solar CellsComparison of Electrolyte and Solid-State Devices. *J. Phys. Chem. B* **2003**, *107* (15), 3556–3564. https://doi.org/10.1021/jp0222144.

(67) Yeum, B. Electrochemical Impedance Spectroscopy: Data Analysis Software, Ann Arbor, MI, USA, 2001.

(68) Cunha, J. M. V.; Rocha, C.; Vinhais, C.; Fernandes, P. A.; Salomé, P. M. P. Understanding the AC Equivalent Circuit Response of Ultrathin Cu(In,Ga)Se$_2$ Solar Cells. *IEEE Journal of Photovoltaics* **2019**, *9* (5), 1442–1448. https://doi.org/10.1109/JPHOTOV.2019.2927918.

(69) Proskuryakov, Y. Y.; Durose, K.; Taele, B. M.; Oelting, S. Impedance Spectroscopy of Unetched CdTe/CdS Solar Cells—Equivalent Circuit Analysis. *Journal of Applied Physics* **2007**, *102* (2), 024504. https://doi.org/10.1063/1.2757011.

(70) Fernandes, P. A.; Sartori, A. F.; Salomé, P. M. P.; Malaquias, J.; da Cunha, A. F.; Graça, M. P. F.; González, J. C. Admittance Spectroscopy of Cu$_2$ZnSnS$_4$ Based Thin Film Solar Cells. *Appl. Phys. Lett.* **2012**, *100* (23), 233504. https://doi.org/10.1063/1.4726042.

(71) Olayiwola, O. I.; Barendse, P. S. Dynamic Equivalent Circuit Modelling of Polycrystalline Silicon Photovoltaic Cells. In *2017 IEEE Energy Conversion Congress and Exposition (ECCE)*; 2017; pp 2310–2317. https://doi.org/10.1109/ECCE.2017.8096449.

(72) Yadav, P.; Pandey, K.; Tripathi, B.; Kumar, M. Investigation of Interface Limited Charge Extraction and Recombination in Polycrystalline Silicon Solar Cell: Using DC and AC Characterization Techniques. *Solar Energy* **2015**, *116*, 293–302. https://doi.org/10.1016/j.solener.2015.04.011.

(73) Tiwari, D.; Koehler, T.; Lin, X.; Sarua, A.; Harniman, R.; Wang, L.; Klenk, R.; Fermin, D. J. Single Molecular Precursor Solution for CuIn(S,Se) $_2$ Thin Films Photovoltaic Cells:

Structure and Device Characteristics. *ACS Appl. Mater. Interfaces* **2017**, *9* (3), 2301–2308. https://doi.org/10.1021/acsami.6b12306.

(74) Roberts, G. I.; Crowell, C. R. Capacitance Energy Level Spectroscopy of Deep-Lying Semiconductor Impurities Using Schottky Barriers. *Journal of Applied Physics* **1970**, *41* (4), 1767–1776. https://doi.org/10.1063/1.1659102.

(75) P-n Junctions 222. In *Physics of Semiconductor Devices*; John Wiley & Sons, Ltd, 2006; pp 77–133. https://doi.org/10.1002/9780470068328.ch2.

(76) Mora-Seró, I.; Garcia-Belmonte, G.; Boix, P. P.; Vázquez, M. A.; Bisquert, J. Impedance Spectroscopy Characterisation of Highly Efficient Silicon Solar Cells under Different Light Illumination Intensities. *Energy Environ. Sci.* **2009**, *2* (6), 678–686. https://doi.org/10.1039/B812468J.

(77) Gupta, G. K.; Garg, A.; Dixit, A. Electrical and Impedance Spectroscopy Analysis of Sol-Gel Derived Spin Coated Cu_2ZnSnS_4 Solar Cell. *Journal of Applied Physics* **2018**, *123* (1), 013101. https://doi.org/10.1063/1.5002619.

(78) Schroder, K. Dieter. Semiconductor Material and Device Characterization, 3rd Edition | Wiley https://www.wiley.com/en-us/Semiconductor+Material+and+Device+Characterization%2C+3rd+Edition-p-9780471739067 (accessed Aug 27, 2020).

(79) Song, S. H.; Nagaich, K.; Aydil, E. S.; Feist, R.; Haley, R.; Campbell, S. A. Structure Optimization for a High Efficiency CIGS Solar Cell. In *2010 35th IEEE Photovoltaic Specialists Conference*; 2010; pp 002488–002492. https://doi.org/10.1109/PVSC.2010.5614724.

(80) Biercuk, M. J.; Monsma, D. J.; Marcus, C. M.; Becker, J. S.; Gordon, R. G. Low-Temperature Atomic-Layer-Deposition Lift-off Method for Microelectronic and Nanoelectronic Applications. *Appl. Phys. Lett.* **2003**, *83* (12), 2405–2407. https://doi.org/10.1063/1.1612904.

(81) Gokmen, T.; Gunawan, O.; Todorov, T. K.; Mitzi, D. B. Band Tailing and Efficiency Limitation in Kesterite Solar Cells. *Appl. Phys. Lett.* **2013**, *103* (10), 103506. https://doi.org/10.1063/1.4820250.

(82) Kuciauskas, D.; Li, J. V.; Contreras, M. A.; Pankow, J.; Dippo, P.; Young, M.; Mansfield, L. M.; Noufi, R.; Levi, D. Charge Carrier Dynamics and Recombination in Graded Band Gap $CuIn_{1-x}Ga_xSe_2$ Polycrystalline Thin-Film Photovoltaic Solar Cell Absorbers. *Journal of Applied Physics* **2013**, *114* (15), 154505. https://doi.org/10.1063/1.4825211.

(83) Kanevce, A.; Levi, D. H.; Kuciauskas, D. The Role of Drift, Diffusion, and Recombination in Time-Resolved Photoluminescence of CdTe Solar Cells Determined through Numerical Simulation. *Progress in Photovoltaics: Research and Applications* **2014**, *22* (11), 1138–1146. https://doi.org/10.1002/pip.2369.

(84) Oueslati, S.; Kauk-Kuusik, M.; Neubauer, C.; Mikli, V.; Meissner, D.; Brammertz, G.; Vermang, B.; Krustok, J.; Grossberg, M. Study of $(Ag_xCu_{1-x})2ZnSn(S,Se)_4$ Monograins Synthesized by Molten Salt Method for Solar Cell Applications. *Solar Energy* **2020**, *198*, 586–595. https://doi.org/10.1016/j.solener.2020.02.002.

(85) Gessert, T. A.; Dhere, R. G.; Duenow, J. N.; Kuciauskas, D.; Kanevce, A.; Bergeson, J. D. Comparison of Minority Carrier Lifetime Measurements in Superstrate and Substrate CdTe PV Devices. In *2011 37th IEEE Photovoltaic Specialists Conference*; 2011; pp 001271–001274. https://doi.org/10.1109/PVSC.2011.6186189.

(86) Hages, C. J.; Redinger, A.; Levcenko, S.; Hempel, H.; Koeper, M. J.; Agrawal, R.; Greiner, D.; Kaufmann, C. A.; Unold, T. Identifying the Real Minority Carrier Lifetime in Nonideal Semiconductors: A Case Study of Kesterite Materials. *Advanced Energy Materials* **2017**, *7* (18), 1700167. https://doi.org/10.1002/aenm.201700167.

(87) Teixeira, J. P.; Salomé, P. M. P.; Alves, B.; Edoff, M.; Leitão, J. P. Evidence of Limiting Effects of Fluctuating Potentials on Cu,In,Ga,Se$_2$ Thin-Film Solar Cells. *Phys. Rev. Applied* **2019**, *11* (5), 054013. https://doi.org/10.1103/PhysRevApplied.11.054013.

(88) Nikolaeva, A.; Krause, M.; Schäfer, N.; Witte, W.; Hariskos, D.; Kodalle, T.; Kaufmann, C. A.; Barreau, N.; Abou-Ras, D. Electrostatic Potential Fluctuations and Light-Soaking Effects in Cu(In,Ga)Se$_2$ Solar Cells. *Progress in Photovoltaics: Research and Applications* **2020**, *n/a* (n/a). https://doi.org/10.1002/pip.3299.

(89) Ghorbani, E.; Kiss, J.; Mirhosseini, H.; Roma, G.; Schmidt, M.; Windeln, J.; Kühne, T. D.; Felser, C. Hybrid-Functional Calculations on the Incorporation of Na and K Impurities into the CuInSe$_2$ and CuIn$_5$Se$_8$ Solar-Cell Materials. *J. Phys. Chem. C* **2015**, *119* (45), 25197–25203. https://doi.org/10.1021/acs.jpcc.5b07639.

(90) Reinhard, P.; Bissig, B.; Pianezzi, F.; Avancini, E.; Hagendorfer, H.; Keller, D.; Fuchs, P.; Döbeli, M.; Vigo, C.; Crivelli, P.; Nishiwaki, S.; Buecheler, S.; Tiwari, A. N. Features of KF and NaF Postdeposition Treatments of Cu(In,Ga)Se$_2$ Absorbers for High Efficiency Thin Film Solar Cells. *Chem. Mater.* **2015**, *27* (16), 5755–5764. https://doi.org/10.1021/acs.chemmater.5b02335.

(91) Handick, E.; Reinhard, P.; Wilks, R. G.; Pianezzi, F.; Kunze, T.; Kreikemeyer-Lorenzo, D.; Weinhardt, L.; Blum, M.; Yang, W.; Gorgoi, M.; Ikenaga, E.; Gerlach, D.; Ueda, S.;

Yamashita, Y.; Chikyow, T.; Heske, C.; Buecheler, S.; Tiwari, A. N.; Bär, M. Formation of a K-In-Se Surface Species by NaF/KF Postdeposition Treatment of Cu(In,Ga)Se$_2$ Thin-Film Solar Cell Absorbers. *ACS applied materials & interfaces* **2017**, *9* (4), 3581–3589. https://doi.org/10.1021/acsami.6b11892.

(92) Yang, P.; Wilks, R. G.; Yang, W.; Bär, M. Interface Formation between CdS and Alkali Postdeposition-Treated Cu(In,Ga)Se$_2$ Thin-Film Solar Cell Absorbers—Key To Understanding the Efficiency Gain. *ACS Appl. Mater. Interfaces* **2020**, *12* (5), 6688–6698. https://doi.org/10.1021/acsami.9b20327.

(93) Weiss, T. P.; Nishiwaki, S.; Bissig, B.; Carron, R.; Avancini, E.; Löckinger, J.; Buecheler, S.; Tiwari, A. N. Injection Current Barrier Formation for RbF Postdeposition-Treated Cu(In,Ga)Se$_2$-Based Solar Cells. *Advanced Materials Interfaces* **2018**, *5* (4), 1701007. https://doi.org/10.1002/admi.201701007.

(94) Salomé, P. M. P.; Rodriguez-Alvarez, H.; Sadewasser, S. Incorporation of Alkali Metals in Chalcogenide Solar Cells. *Solar Energy Materials and Solar Cells* **2015**, *143*, 9–20. https://doi.org/10.1016/j.solmat.2015.06.011.

(95) Kirchartz, T.; Ding, K.; Rau, U. Fundamental Electrical Characterization of Thin-Film Solar Cells. In *Advanced Characterization Techniques for Thin Film Solar Cells*; John Wiley & Sons, Ltd, 2011; pp 33–60. https://doi.org/10.1002/9783527636280.ch2.

(96) Rau, U. Tunneling-Enhanced Recombination in Cu(In, Ga)Se$_2$ Heterojunction Solar Cells. *Appl. Phys. Lett.* **1999**, *74* (1), 111–113. https://doi.org/10.1063/1.122967.